ARTICLES
PUBLISHED ONLINE: 19 APRIL 2009 | DOI: 10.1038/NMAT2429
nature materials

Enhancement of ferroelectricity at metal–oxide interfaces

Massimiliano Stengel[1], David Vanderbilt[2] and Nicola A. Spaldin[1]*

The development of ultrathin ferroelectric capacitors for use in memory applications has been hampered by depolarization effects arising from the electrode–film interfaces. These can be characterized in terms of a reduced interface capacitance, or equivalently an 'effective dead layer' in contact with the electrode. Here, by performing first-principles calculations on four capacitor structures based on $BaTiO_3$ and $PbTiO_3$, we determine the intrinsic interfacial effects responsible for destabilizing the ferroelectric state in ultrathin-film devices. Although it has been widely believed that these are governed by the electronic screening properties at the interface, we show that they also depend crucially on the local chemical environment through the force constants of the metal oxide bonds. In particular, in the case of interfaces formed between AO-terminated perovskites and simple metals, we demonstrate a novel mechanism of interfacial ferroelectricity that produces an overall enhancement of the ferroelectric instability of the film, rather than its suppression as is usually assumed. The resulting 'negative dead layer' suggests a route to thin-film ferroelectric devices that are free of deleterious size effects.

Capacitors based on ferroelectric perovskites are potentially attractive for applications in nanoelectronics, such as non-volatile random-access memories and high-permittivity gate dielectrics. Thin-film geometries are sought for optimal efficiency and information storage density[1]. However, in the thin-film regime, strong size-dependent effects arise. These can considerably worsen the attractive functionalities of the ferroelectric material by, for example, reducing the dielectric response[2,3] and causing rapid polarization relaxation[4]. Understanding and addressing these deleterious effects is crucial for future progress[5].

Several hypotheses have been formulated to interpret size effects in thin-film ferroelectric capacitors. Usually the experimental data can accurately be described in terms of the 'series capacitor model', where the overall capacitance C of the device is written as

$$\frac{1}{C} = \frac{1}{C_1} + \frac{4\pi t}{\epsilon_b S} + \frac{1}{C_2} \qquad (1)$$

Here ϵ_b is the bulk permittivity of the dielectric material of thickness t, $C_{1,2}$ are capacitances associated with low-permittivity layers located at the film–electrode interfaces and S is the surface area. Such interfacial capacitances produce a depolarizing field[6,7] that strongly reduces the dielectric response in the paraelectric regime and can destabilize the single-domain ferroelectric state. An accurate knowledge of the interfacial capacitance and its dependence on the combination of ferroelectric and electrode materials is, therefore, crucial for device design.

Interestingly, such interfacial 'dead layers' are present even in high-quality epitaxial systems, where the defect density is very low[4]. This suggests possible fundamental issues affecting the polarization at the metal/ferroelectric boundary. In particular, within the Thomas–Fermi model, many authors focus on the imperfect compensation of the polarization charges due to the finite electronic screening length of metallic electrodes. To explain the substantially better performance of $SrRuO_3$ (SRO) electrodes as compared with Pt ones, as has been observed experimentally[2,3], one can then invoke the lattice contribution to the screening, which is expected to be significant[8] in oxide electrodes.

The above interpretation, however, is clearly unsatisfactory at the microscopic level. The region where the interface effects occur is as thin as a few interatomic spacings[9]. In this region the local chemical and electrostatic environment departs significantly from that of either parent material, and a description of the interface in terms of bulk parameters is unjustified[5]. To describe such effects, a full quantum-mechanical treatment is required.

First-principles calculations have already been invaluable in understanding the properties of nanoscale ferroelectrics. Early work established the suitability of the methods for studying surface and interface properties and for obtaining a microscopic picture of electrostatic effects[10–12]. More recent studies have focused on the effects of strain[13,14] and interfacial electrostatics[6,15,16] in determining the spontaneous polarization of symmetric[17] or asymmetric[18] capacitor geometries with various ferroelectric–electrode combinations. Most authors agree on the existence of a depolarizing field, caused by imperfect screening at the interface, which tends to suppress single-domain ferroelectricity. It is now generally accepted that the imperfect screening is a property of the interface as a whole (that is, the metal, the ferroelectric and the specific interface geometry), which requires consideration of an effective screening length, λ_{eff}, rather than the Thomas–Fermi one[5]. However, a clear description of the microscopic mechanisms determining λ_{eff} has not yet emerged. The recent development of rigorous first-principles methods to define and control the polarization in a metal–ferroelectric heterostructure[19,20] now provides the opportunity to perform such analysis.

In the present work we concentrate on ultrathin ferroelectric capacitor structures in which the ferroelectric is $PbTiO_3$ (PTO) or $BaTiO_3$ (BTO) and the metallic electrode can be SRO or Pt. Aside from being technologically relevant combinations, these are diverse enough to cover several kinds of behaviour while remaining focused enough to enable an in-depth analysis. We find that the interfacial dielectric response is more complex than usually assumed in phenomenological models, where only the

[1]Materials Department, University of California, Santa Barbara, California 93106-5050, USA, [2]Department of Physics and Astronomy, Rutgers University, Piscataway, New Jersey 08854-8019, USA. *e-mail: nicola@mrl.ucsb.edu.

Table 1 | Calculated inverse capacitance densities $C^{-1}S$, interfacial inverse capacitance densities $C_i^{-1}S$, critical thicknesses N_{crit} and effective screening lengths λ_{eff} for the four capacitor heterostructures discussed in this work.

	N	$C^{-1}S$ (m^2 F^{-1})	$C_i^{-1}S$ (m^2 F^{-1})	N_{crit}	λ_{eff} (Å)
BTO–SRO	6.5	−1.553	2.280	4.85	0.202
PTO–SRO	6.5	0.439	1.727	7.45	0.153
STO–SRO*	6.5	3.876	1.647	—	0.146
PTO–Pt	8.5	−1.427	1.258	5.42	0.111
BTO–Pt	8.5	−7.920	0.037	0.08	0.003

*Data for STO–SRO are from ref. 22.

penetration of the electric field into the electrode is considered. In particular, we develop a rigorous theory, based on the modern theory of polarization, in which the interface-specific effects of purely electronic screening and of interatomic force constants are both taken fully into account in assessing the overall performance of the capacitor. Based on our analysis, we demonstrate a covalent bonding mechanism that yields a ferroelectric behaviour of the interface between AO-terminated films and simple metals. In this case one finds an overall enhancement of the driving force of the film towards a polar state, rather than a suppression as is predicted by semiclassical theories.

Approach

Our calculations are performed within the local-density approximation of density-functional theory and the projector-augmented-wave method[21] as implemented in an in-house code. An isolated capacitor with semi-infinite leads is modelled by a periodic array of alternating metallic and insulating layers, where the thickness of the metallic slab is treated as a convergence parameter and the ferroelectric film is N unit cells thick (the actual values are reported in Table 1). We focus on symmetric interface terminations of the SrO–TiO_2 type for SRO electrodes, and of the Pt_2–AO type for Pt electrodes. (Note that some other authors have considered the structurally dissimilar Pt_2–TiO_2 interface instead; the arguments developed in this work are very general and could be readily extrapolated to that case.) In all cases we constrain the in-plane lattice parameter to the theoretical bulk $SrTiO_3$ value. We use our recently developed fixed-D (ref. 20) method, combined with the extensions to metal–insulator heterostructures of refs 19 and 22, to analyse the linear response of the paraelectric structure to a small polar perturbation. This regime is relevant for the existence of a (meta)stable single-domain ferroelectric state, and allows for a microscopic analysis of the physical ingredients contributing to the screening, without complications arising from asymmetries or pathological band alignments[5].

To assess the stability of a given structure against a polar distortion, we are concerned with C^{-1}, its inverse capacitance per in-plane unit cell, which can be expressed as[20]

$$C^{-1} = \left(\frac{4\pi}{S}\right)^2 \frac{\mathrm{d}^2 U}{\mathrm{d}D^2} = -\frac{4\pi}{S}\frac{\mathrm{d}V}{\mathrm{d}D} \qquad (2)$$

where U is the internal energy per in-plane cell, S is the cell area, V is the potential drop across the capacitor plates and D is the electric displacement. We note that C^{-1} is a 'generalized' inverse capacitance that is meaningful even when it is negative[20], in which case it signals the appearance of an instability to a ferroelectric distortion in the capacitor arrangement—the more negative, the stronger the driving force towards a polar state.

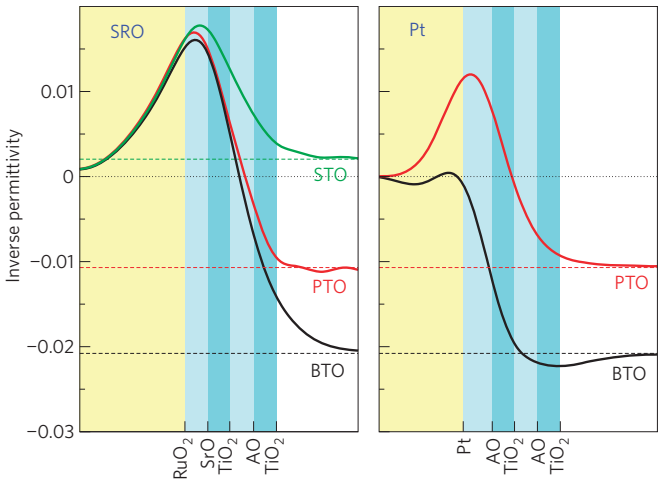

Figure 1 | Inverse local permittivity profiles for symmetric capacitor structures studied in this work. (For the SRO electrode, the STO curve from ref. 22 is added for comparison.) Inverse permittivities calculated for bulk STO, BTO and PTO are shown as dashed horizontal lines. Electrodes and oxide layers closest to the interface are indicated by shading.

We calculated C^{-1} for the four capacitor heterostructures considered in this work using a finite-difference approach. In particular, for each system we performed two complete electronic and structural relaxations, first at $D = 0$ by imposing a mirror symmetry, and then at $D = 0.001$ a.u. (a value that is small enough to ensure linearity) using our finite-field technique[19,20]. This is possible because the fixed-D method enables us to define and compute the equilibrium state of an insulating system, within a given set of symmetry constraints and at a given value of macroscopic D, even in configurations that would be unstable at fixed electric field (for example a ferroelectric near the saddle point of its double-well potential). Finally, we extracted the induced bias potential and discretized equation (2) to obtain the inverse capacitances, whose values are reported in Table 1. The positive sign of C^{-1} in the PTO–SRO case indicates that the system is paraelectric for the considered PTO thickness, whereas the other structures are in the ferroelectric regime.

A quantity that has received considerable attention in the recent past[6,15–17] is the critical thickness for ferroelectricity, defined as the minimum thickness for which a uniform polar state exists. The usual strategy to determine this quantity computationally is to perform several calculations for varying thicknesses until a spontaneous polarization appears. Instead, we find it much more convenient to exploit the power of the fixed-D approach and obtain such information directly from a calculation on a single thickness.

To this end, it is useful to look first at the spatial decomposition of the inverse capacitances shown in Fig. 1, where we plot the local inverse permittivity profiles $\epsilon^{-1}(x) = \mathrm{d}\bar{E}(x)/\mathrm{d}D$ (evaluated at $D = 0$), where $\bar{E}$ is the x component of the y–z-averaged electric field along the stacking direction x. (These are calculated as in ref. 22, except that our use here of the fixed-D method enables treatment of cases with $C^{-1} < 0$.) The profiles are generally characterized by two regions: an interfacial part, where the imperfect screening manifests itself as a positive peak in $\epsilon^{-1}(x)$, and the deep interior of the insulating film, where $\epsilon^{-1}(x)$ converges to the bulk value.

This naturally suggests a local decomposition between interface and bulk effects, where the overall stability of the centrosymmetric state emerges from the competition between these two usually opposite contributions. By defining $C_b^{-1} = 4\pi c_b/(\epsilon_b S)$ as the bulk inverse capacitance per unit cell (c_b is the cell parameter along the

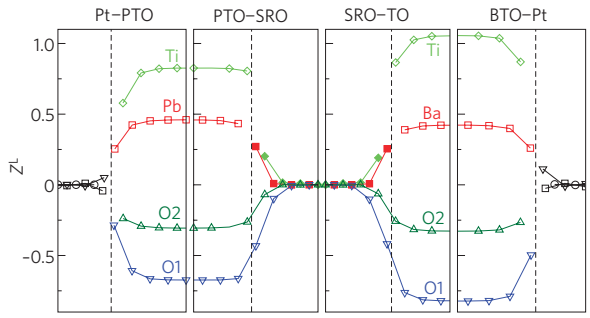

Figure 2 | Plots of Callen dynamical charges, arranged head to head and tail to tail to emphasize rapid convergence to common bulk values. Coloured symbols denote A-site cations (red squares), B-site cations (light-green diamonds), AO oxygens (O1, blue down triangles) and BO_2 oxygens (O2, dark-green up triangles). The Pt atoms (black symbols) are labelled according to their projection onto the interface plane. Of the four independent Pt sites, one is shared with the A cations (squares), another is shared with O1 (down triangles) and the remaining two, equivalent by symmetry, are shared with O2 (circles).

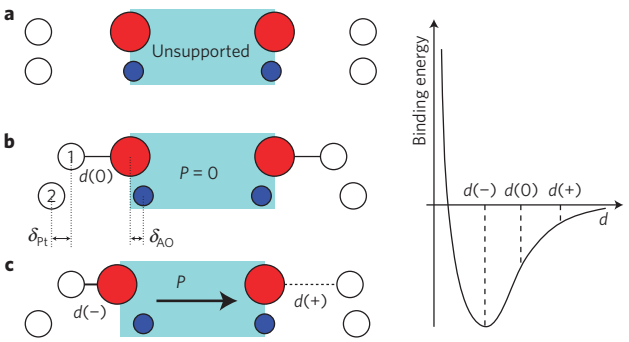

Figure 3 | Schematic representation of the salient features of the Pt_2–AO interface. Only interfacial atoms are shown; open, red and blue circles denote Pt, O and A atoms respectively. **a**, Unsupported film and metal surfaces. A small surface rumpling is present only in the AO surface layer whereas the metal is flat. **b**, Centrosymmetric interface geometry, with significant rumplings δ, especially in the Pt_2 layer. **c**, Proposed mechanism for interfacial ferroelectricity, driven by the unstable Pt-O bond. Right: example of a two-body binding energy curve with negative curvature at $d(0)$.

field direction), and N as the thickness of the film in bulk cells, we rewrite equation (1) as

$$C^{-1} = C_1^{-1} + C_2^{-1} + NC_b^{-1}$$

The inversion symmetry of our paraelectric capacitor heterostructures then implies $C_1 = C_2 = C_i$, which leads to

$$C_i^{-1} = \frac{C^{-1} - NC_b^{-1}}{2} \tag{3}$$

In the general case where the symmetry is broken on ferroelectric off-centring (or by adopting structurally inequivalent interfaces), C_1 and C_2 must be resolved individually. This is still possible within the present methodology, although the procedure is slightly more involved. We take equation (3) to be our definition of the interfacial inverse capacitance. (Note that the definition depends on the precise convention for specifying N; we adopt the convention that N is the nominal thickness as illustrated by the examples in Table 1.) Then, given C_i^{-1} and C_b^{-1}, we again use equation (1) to predict the critical thickness

$$N_{crit} = -\frac{2C_i^{-1}}{C_b^{-1}} \tag{4}$$

for ferroelectricity, this being the value of N that yields an overall vanishing inverse capacitance (that is, $C^{-1} = 0$). For an interface to a ferroelectric material ($C_b^{-1} < 0$), it is also natural to define the effective dead-layer thickness $N_{dead} = -C_i^{-1}/C_b^{-1}$, in terms of which

$$N_{crit} = 2N_{dead}$$

Results

The calculated values for C_i^{-1} and N_{crit} are reported in Table 1, together with the values already calculated in ref. 22 for paraelectric $SrTiO_3$ (STO) between SRO electrodes. Since many authors[5] discuss interfacial effects in terms of effective screening lengths $\lambda_{eff} = C_i^{-1}S/4\pi$ rather than capacitances, we also report these values in Table 1.

Our numbers are overall consistent with the published literature data, keeping in mind that different approximations, for example the use of the local-density versus the generalized-gradient approximation, might cause a significant degree of variability at the quantitative level. For example, ref. 6 found $N_{crit} = 6$ for BTO–SRO, which is larger than our value of about 5; however, ionic relaxations (which were ignored there) tend to decrease N_{crit} significantly[17], and would probably improve the agreement. For the same system, the authors of ref. 17 found $N_{crit} = 3$, this time smaller than our value, but a generalized-gradient approximation functional (which tends to overestimate ferroelectric effects) was used there instead of the local-density approximation. Similar discrepancies related to the choice of the functional apply to the PTO–Pt capacitors discussed in refs 15 and 16; our results agree reasonably well with the local-density approximation values presented in ref. 16.

It is rather surprising that the calculated N_{crit} of BTO–SRO is smaller than that of PTO–SRO. Indeed, PTO has a much larger spontaneous polarization P_s in the tetragonal ground state than BTO, and it would be tempting to think that the former is a 'stronger' ferroelectric and therefore should have a smaller critical thickness. The calculated trend in N_{crit} is even more surprising on observing that C_i^{-1} of PTO–SRO is smaller than that of BTO–SRO, which would favour the opposite trend. It is clear from equation (4), however, that $|C_b^{-1}|$, rather than P_s, is the parameter that defines the strength of the bulk ferroelectric instability; at the fixed STO in-plane lattice constant, our calculated $|C_b^{-1}|$ is about twice as large in BTO as in PTO, which agrees nicely with the trend in N_{crit}. This highlights once again the fact that the 'switchability' (quantified by the inverse capacitance $|C^{-1}|$), rather than the 'polarity' P_s, is the relevant property that characterizes the stability of the ferroelectric state.

In the Pt-based systems considered here, λ_{eff} is systematically smaller than in the SRO-based systems, in stark contrast with the predictions of the semiclassical models of refs 8 and 23. (First-principles calculations have already demonstrated, in the case of STO paraelectric capacitors, that Pt electrodes can be intrinsically superior to SRO electrodes[22].) While λ_{eff} is still significant in PTO–Pt, in the case of BTO–Pt it practically vanishes, or equivalently the dead-layer thickness of $N_{dead} = 0.04$ layers is almost zero! To validate this result, we carried out calculations on a BTO–Pt capacitor structure containing only a single unit cell of BTO, and confirmed that this structure is still unstable to ferroelectric distortion. This suggests that novel effects must take place at this interface that go beyond the usual Thomas–Fermi arguments, which always predict the same positive value of λ_{eff} independent of the ferroelectric material.

Table 2 | Computed structural parameters for Pt_2–AO interfaces.

System	d (Å)	δ_{Pt} (Å)	δ_{AO} (Å)
BTO–Pt	2.26	0.46	0.12
PTO–Pt	2.11	0.34	0.19

See Fig. 3 for the definition of the symbols.

To investigate the origin of this unexpected behaviour, we perform a microscopic analysis of the electrostatic response to a D field in the two Pt-based capacitors. The static inverse capacitance can be decomposed as

$$C^{-1} = (C^{\infty})^{-1} - \Delta \quad (5)$$

where $(C^{\infty})^{-1}$ is the purely electronic, frozen-ion value and $-\Delta$ is the lattice-mediated contribution. The latter can be expressed in terms of the Callen (or longitudinal) dynamical charge tensor Z^{L} (ref. 24), and the longitudinal force constant matrix $\mathbf{K}^{L}$, as

$$\Delta = \left(\frac{4\pi}{S}\right)^{2} \sum_{ij} Z^{L}_{i,x} (K^{L})^{-1}_{ij} Z^{L}_{j,x} \quad (6)$$

where x is again the stacking direction (see the Methods section for the formal derivation). Note that the sums in equation (6) run over all atoms in principle, including those located deep in the metallic electrodes, but in practice these do not contribute because their dynamical charges are zero (see Fig. 2). The convenience of using equation (6) instead of the usual decomposition involving transverse quantities (for example equation (8) of ref. 25) is that, in a layered heterostructure, $\mathbf{K}^{L}$ is short ranged in real space[26,27]. This means that local bonding effects can be unambiguously separated from the long-range electrostatic interactions, thus allowing for a detailed analysis of the microscopic mechanisms contributing to the polarization.

Discussion

The dissimilar behaviour of PTO–Pt and BTO–Pt could be due, in principle, to variations in the purely electronic term $(C^{\infty})^{-1}$. These might stem from different penetration lengths of the electric fields and metallic wavefunctions at the interface. The calculated value of C^{∞} for PTO–Pt and BTO–Pt can be quantified in terms of an effective dielectric thickness, N^{∞}, defined as

$$N^{\infty} = \frac{\epsilon_{b}^{\infty} S}{4\pi c_{b} C^{\infty}}$$

where ϵ_{b}^{∞} is the high-frequency permittivity of the bulk insulator. We obtain $N^{\infty} = 8.18$ in BTO–Pt, and $N^{\infty} = 7.75$ in PTO–Pt. This means that the purely electronic screening is even better at the PTO–Pt interface than at the BTO–Pt interface, and indicates that mechanisms driven by ionic relaxations must be entirely responsible for the vanishing dead layer in BTO–Pt.

It is clear from equation (6) that two basic ingredients contribute to the ionic polarizability: the force constants contained in $\mathbf{K}^{L}$, and the dynamical charge associated with a given degree of freedom, Z^{L}. Since the inverse of $\mathbf{K}^{L}$ enters the sum, it is obvious that less stable bonds will yield an enhanced response, provided that the participating atoms carry a significant Z^{L}. It is reasonable then to expect that the relative weakness of the bonds formed by the ferroelectric films with Pt, compared with those formed with the isostructural conducting oxide SRO, might explain the enhanced interfacial dielectric properties of the former

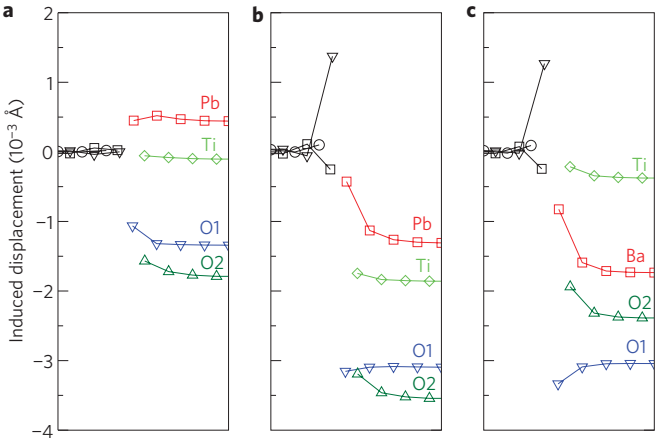

Figure 4 | Ionic displacements induced by a small field of $D = 10^{-3}$ a.u. (0.455 μC cm^{-2}). a, PTO-Pt; **b**, PTO-Pt modified by artificial addition of force constant $k = -0.05$ a.u.; **c**, BTO-Pt. The colour-symbol scheme is the same as in Fig. 2. The horizontal axis is the x coordinate, normal to the interface plane, and refers to the relaxed atomic positions in the centrosymmetric geometry.

electrode material, and possibly the qualitative difference between PTO–Pt and BTO–Pt.

To investigate this hypothesis, we start by looking at the relaxed geometry of the interfacial Pt_2 and AO layers when the film is in the centrosymmetric configuration (Fig. 3). The significant rumpling δ, which is present in both Pt_2 and AO (Table 2), brings Pt(1) and the interface O atoms into much closer contact than the neighbouring Pt(2) and A cations, indicating that only the former two atoms form a true chemical bond[12]. Moreover, the strong buckling in the Pt_2 layer is indicative of a frustrated bonding environment, where the repulsive A–Pt interaction is in competition with the attractive O–Pt bond. As a result, the O–Pt distance d in the relaxed interface structures is in both cases significantly larger than the typical Pt–O equilibrium distance of about 2.0 Å, which has been determined experimentally and theoretically in a number of bulk oxide phases[28]. Comparing the interface systems, d is even larger in BTO–Pt than in PTO–Pt, indicating that the Pt–O bond is weaker in the former system.

To quantify this difference in strength, we examine the local force constants characterizing the Pt–O interfacial bond. At the PTO–Pt interface we have $K^{L}_{Pt-O} = -0.039$ a.u., which is comparable to the typical interatomic force constants in oxide crystals and is consistent with a stable chemical bond. Strikingly, at the BTO–Pt interface we have $K^{L}_{Pt-O} = 0.001$ a.u., a very small and positive value, which indicates that the Pt–O bond here is slightly unstable (that is, there is no restoring force associated with it). This indicates that the structural frustration present at the interface is strong enough in BTO–Pt to pull the Pt–O bond into an unstable regime (see Fig. 3, right). This qualitative difference between PTO–Pt and BTO–Pt is entirely responsible for their inequivalent polar responses, as we shall see in the following.

To link the stability of the Pt(1)–O bond to the dielectric response of the capacitor, we perform a computational experiment in which we artificially modify the force-constant matrices $\mathbf{K}^{L}$ of PTO–Pt and BTO–Pt by adding a negative harmonic term of the form $E_{h} = (k/2)[|x_{O} - x_{Pt}| - d(0)]^{2}$ between Pt(1) and O, which weakens the corresponding bond without changing the centrosymmetric equilibrium geometry. Our goal is to demonstrate that, by choosing an appropriate value of k, we can destabilize the Pt(1)–O bond at the PTO–Pt interface and therefore reproduce the behaviour (dead-layer thickness and atomic displacement pattern) of the BTO–Pt system. To this end, we choose $k = -0.05$ a.u. (a value slightly larger than K^{L}_{Pt-O}) and

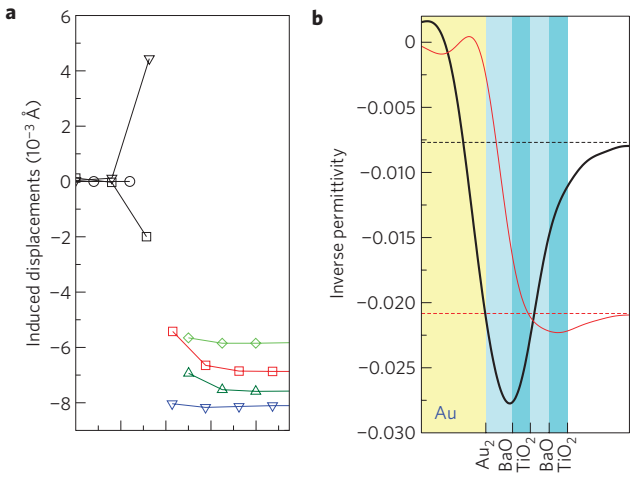

Figure 5 | Computed local properties at the BTO–Au interface. a, Ionic displacements induced by a small field of $D = 0.001$ a.u. **b**, Inverse permittivity profile (thick solid black curve) compared with corresponding BTO–Pt results (thin solid red curve) as in Fig. 1. The thin dashed lines in **b** indicate the values of the bulk inverse permittivity of BTO at $D = 0$ for two different values of the in-plane strain, 0% (black) and −2.2% (red), corresponding to the cubic lattice constants of BTO and STO, respectively.

we recalculate the effective dead-layer thickness for PTO–Pt by inserting this modified $\mathbf{K}^{L}$ matrix into equation (6). Remarkably, owing to the additional harmonic term E_h, $N_{dead} = 2.71$ jumps to a very small value $N_{dead} = 0.08$, practically identical to that of the unmodified BTO–Pt case.

To further prove that the 'modified' PTO–Pt behaves in all important respects like BTO–Pt, we plot in Fig. 4 the induced ionic displacements in three different cases: PTO–Pt ($k = 0$), PTO–Pt ($k = -0.05$) and BTO–Pt ($k = 0$). Note that the ionic responses to a small D field are very different in the first and last cases. In this context, it is remarkable that the middle 'modified PTO–Pt' case is strikingly similar to BTO–Pt, even in many fine details of the induced relaxations at the interface layers. Deeper into the oxide, the displacements reflect the different ferroelectric mode patterns (for example, there is a larger displacement for Pb than for Ba because of the stereochemical activity of the Pb lone pairs), but the behaviour of the first oxide layers is nearly identical. This unambiguously demonstrates that the dissimilar behaviour in the BTO–Pt and PTO–Pt cases is almost entirely due to the change in stability of the Pt–O bond.

Now, to have a mechanism for ferroelectricity, a structural instability needs to be coupled to the polarization. Comparing the original and the 'modified' PTO–Pt ionic displacement patterns in Fig. 4a,b, it is apparent that the stretching of the Pt–O bond is associated with (1) a shift of the whole ferroelectric slab in the opposite direction to D and (2) a combined rumpling of the AO and Pt_2 layers. Since the atoms in both Pt_2 and AO carry significant values of Z^{L} (see Fig. 2), both effects have a strong impact on the polarization. We therefore identify this mechanism as a novel form of 'interfacial ferroelectricity.' Here we have a flagrant breakdown of phenomenological models based on bulk properties of the parent materials.

These arguments lead to a rather general prediction, namely that AO-terminated perovskite ferroelectrics can show a strong interfacial enhancement of the ferroelectric properties when weakly bonded to a simple metal. To test this prediction, we performed a supplementary calculation for a BTO-based capacitor with the Pt electrodes replaced by a more inert material, Au. In this case the equilibrium lattice constant of bulk BTO was used for the epitaxial strain constraint, to better match the experimental set-up of ref. 29, but otherwise all computational parameters were kept the same. As before, we first relaxed the centrosymmetric geometry and then calculated the ionic and electronic response to a small field. The calculated induced ionic displacements for BTO–Au, presented in Fig. 5a, show the same qualitative features (1) and (2) discussed above, but their magnitude is about four times larger than in BTO–Pt, reflecting the weaker Au–oxide interaction. Consistent with the enhanced displacements, we obtain a negative dead-layer thickness of $N_{dead} = -5.5$ layers, which manifests itself as an unusually large dip in the local permittivity profile, shown in Fig. 5b. (Note the rather dissimilar bulk 'ferroelectric strength' of BTO at the different in-plane strain states.) In other words, the actual capacitor with 8.5 layers of BTO and real Au electrodes has the same degree of ferroelectric instability as ∼19.5 layers of BTO between 'ideal' electrodes! It is quite remarkable that such a huge effect can be caused by only two atomic monolayers at the interface (Au_2 and BaO). Note that an interface-induced enhancement of ferroelectricity in thin films has already been proposed in the context of Landau theory[30] and the effective Hamiltonian approach[31]; the present work demonstrates how these ideas can be realized in the framework of realistic first-principles calculations for specific materials.

Before concluding, we briefly discuss the relation between the ferroelectric instability at $D = 0$, which has been our main concern above, and the spontaneous polarization that develops in the fully relaxed capacitor in short circuit. Interestingly, we find rather different behaviour for the BTO–Pt and BTO–Au cases. For a seven-unit-cell-thick film of BTO between Pt electrodes, we obtain a polarization $P = 0.45\,C\,m^{-2}$, which is about 15% larger than the spontaneous polarization $P_s = 0.39\,C\,m^{-2}$ calculated for bulk $BaTiO_3$ epitaxially constrained to the $SrTiO_3$ lattice parameter. In fact, we find enhanced ferroelectric distortions even for the case of a single unit cell of BTO between Pt electrodes. These tests indicate that the covalent bonding effects discussed for BTO–Pt become even stronger at the interfaces of the fully polarized capacitor. However, a similar test for a BTO film between Au electrodes yielded a polarized state of the film that was essentially bulk-like. Here, the strong enhancement of the instability does not translate into an enhancement in the polarity, again indicating that these two phenomena are not necessarily correlated.

Outlook

Our calculations demonstrate a strong correlation of the overall ferroelectric response of a capacitor to the stiffness of the electrode–oxide bonds. We predict an enhancement in the ferroelectric instability of the film whenever these bonds are unstable in the centrosymmetric reference structure. This result opens exciting new avenues for engineering the electrical properties of thin-film devices by exploiting the rich chemistry of metal–oxide interfaces. By using appropriate growth conditions, it may be well within the realm of possibility (although certainly challenging) to directly control the structure and termination of perovskite/simple metal interfaces, and thus take advantage of the effects described here. We hope that our theory will motivate experimental efforts in this direction.

Methods

Our calculations are performed within the local-density approximation of density-functional theory and the projector-augmented-wave method[21], with a plane-wave-basis cutoff energy of 40 Ryd. We constrain the in-plane lattice constant to the calculated theoretical equilibrium value for cubic $SrTiO_3$ ($a = 7.276$ a.u.) unless otherwise specified. We set the thickness of the insulating film to N unit cells (the actual values are reported in Table 1). The thickness of the metal electrode slab was 7.5 unit cells of SRO or 11 atomic layers of Pt, which were sufficient to converge the interface properties of interest. We use a 6×6 Monkhorst–Pack sampling of the surface Brillouin zone, which reduces to six special points within the tetragonal symmetry. A Gaussian smearing of 0.15 eV was used to accelerate convergence of the Brillouin-zone integrations. We carefully checked that the band alignment at the interface and the choice of the smearing scheme is such that any

spurious population of the conduction band of the insulating film is avoided. All the structural degrees of freedom were fully relaxed subject to the translational and point symmetries (a mirror symmetry plane is first imposed to relax the geometry in the paraelectric state, and later relaxed when calculating the linear response to a displacement field).

The insulating character of the system along the stacking direction (the insulator is thick enough that direct tunnelling is suppressed) allows for a rigorous definition of the macroscopic polarization and its coupling to an external bias voltage[19,22]. Because at the quantum-mechanical level all wavefunctions are mutually coupled and there is no clear way to separate free conduction charge from the bound polarization charge, we adopt the convention of treating all charges as bound charges, so that D is a constant throughout the heterostructure just as for a purely insulating system[32]. (Strictly speaking, D and P here are the longitudinal components of the respective fields.) What would customarily be called the macroscopic free charge σ on the top of the electrode is here reinterpreted as a bound charge associated with a polarization $P=\sigma$ in the metallic region. (Indeed $D=4\pi\sigma$, because the electric field must vanish in the metallic region.)

All quantities requiring a derivative with respect to D were performed by finite differences between a calculation with mirror symmetry imposed ($D=0$) and a fixed-D calculation with $D=0.001$ a.u. The longitudinal force-constant matrices and the dynamical charges were computed by finite differences by taking displacements of 0.4 mÅ along the tetragonal axis.

The expression for the inverse capacitance in equations (5) and (6) was derived as follows. We start by considering the internal energy $U(D)$, which depends on the electric displacement D explicitly and also implicitly through the active ionic degrees of freedom x_i,

$$U(D)=U(\{x_i(D)\},D)$$

Then the total derivative in equation (2) can be expanded as

$$\frac{\mathrm{d}^2U}{\mathrm{d}D^2}=\frac{\partial^2U}{\partial D^2}+\sum_i\frac{\partial^2U}{\partial D\partial x_i}\frac{\partial x_i}{\partial D} \qquad (7)$$

The first term on the right-hand side is proportional to the frozen-ion inverse capacitance $(C^{\infty})^{-1}$. The second derivative of U in the sum is minus the Callen charge Z_i^{L} associated with the ith degree of freedom. Finally, the induced displacements $\partial x_i/\partial D$ can be written in terms of the inverse longitudinal force-constant matrix, $(\mathbf{K}^{\mathrm{L}})^{-1}$, multiplied by the Callen charges. Hence, by combining equations (2) and (7), equations (5) and (6) immediately follow.

Received 5 November 2008; accepted 18 March 2009; published online 19 April 2009

References

1. Dawber, M., Rabe, K. M. & Scott, J. F. Physics of thin-film ferroelectric oxides. *Rev. Mod. Phys.* **77**, 1083–1130 (2005).
2. Hwang, C. S. Thickness-dependent dielectric constant of (Ba,Sr)TiO_3 thin films with Pt or conducting oxide electrodes. *J. Appl. Phys.* **92**, 432–437 (2002).
3. Plonka, R., Dittmann, R., Pertsev, N. A., Vasco, E. & Waser, R. Impact of the top-electrode material on the permittivity of single-crystalline $Ba_{0.7}Sr_{0.3}TiO_3$ thin films. *Appl. Phys. Lett.* **86**, 202908 (2005).
4. Kim, D. J. *et al.* Polarization relaxation induced by a depolarization field in ultrathin ferroelectric $BaTiO_3$ capacitors. *Phys. Rev. Lett.* **95**, 237602 (2005).
5. Junquera, J. & Ghosez, P. First-principles study of ferroelectric oxide epitaxial thin films and superlattices: Role of the mechanical and electrical boundary conditions. *J. Comput. Theor. Nanosci.* **5**, 2071–2088 (2008).
6. Junquera, J. & Ghosez, P. Critical thickness for ferroelectricity in perovskite ultrathin films. *Nature* **422**, 506–509 (2003).
7. Pertsev, N. A., Dittmann, R., Plonka, R. & Waser, R. Thickness dependence of the intrinsic dielectric response and apparent interfacial capacitance in ferroelectric thin films. *J. Appl. Phys.* **86**, 202908 (2005).
8. Black, C. T. & Welser, J. J. Electric-field penetration into metals: Consequences for high-dielectric constant capacitors. *IEEE Trans. Electron Devices* **46**, 776–780 (1999).
9. Tagantsev, A. K. & Gerra, G. Interface-induced phenomena in polarization response of ferroelectric thin films. *J. Appl. Phys.* **100**, 051607 (2006).
10. Cohen, R. E. Periodic slab LAPW computations for ferroelectric $BaTiO_3$. *J. Phys. Chem. Sol.* **57**, 1393–1396 (1996).
11. Cohen, R. E. Surface effects in ferroelectrics: Periodic slab computations for $BaTiO_3$. *Ferroelectrics* **194**, 323–342 (1997).
12. Rao, F. Y., Kim, M. Y., Freeman, A. J., Tang, S. P. & Anthony, M. Structural and electronic properties of transition-metal/$BaTiO_3$(001) interfaces. *Phys. Rev. B* **55**, 13953–13960 (1997).
13. Rabe, K. M. Theoretical investigations of epitaxial strain effects in ferroelectric oxide thin films and superlattices. *Curr. Opin. Solid State Mater. Sci.* **9**, 122–127 (2005).
14. Ederer, C. & Spaldin, N. A. Effect of epitaxial strain on the spontaneous polarization of thin film ferroelectrics. *Phys. Rev. Lett.* **95**, 257601 (2005).
15. Sai, N., Kolpak, A. M. & Rappe, A. M. Ferroelectricity in ultrathin perovskite films. *Phys. Rev. B* **72**, 020101(R) (2005).
16. Umeno, Y., Meyer, B., Elsässer, C. & Gumbsch, P. Ab initio study of the critical thickness for ferroelectricity in ultrathin Pt/$PbTiO_3$/Pt films. *Phys. Rev. B* **74**, 060101(R) (2006).
17. Gerra, G., Tagantsev, A. K., Setter, N. & Parlinski, K. Ionic polarizability of conductive metal oxides and critical thickness for ferroelectricity in $BaTiO_3$. *Phys. Rev. Lett.* **96**, 107603 (2006).
18. Gerra, G., Tagantsev, A. K. & Setter, N. Ferroelectricity in asymmetric metal–ferroelectric–metal heterostructures: A combined first-principles–phenomenological approach. *Phys. Rev. Lett.* **98**, 207601 (2007).
19. Stengel, M. & Spaldin, N. A. Ab-initio theory of metal–insulator interfaces in a finite electric field. *Phys. Rev. B* **75**, 205121 (2007).
20. Stengel, M., Spaldin, N. A. & Vanderbilt, D. Electric displacement as the fundamental variable in electronic-structure calculations. *Nature Phys.* **5**, 304–308 (2009).
21. Blöchl, P. E. Projector augmented-wave method. *Phys. Rev. B* **50**, 17953–17979 (1994).
22. Stengel, M. & Spaldin, N. A. Origin of the dielectric dead layer in nanoscale capacitors. *Nature* **443**, 679–682 (2006).
23. Choi, W. S. *et al.* Dielectric constants of Ir, Ru, Pt, and IrO_2: Contributions from bound charges. *Phys. Rev. B* **74**, 205117 (2006).
24. Ghosez, P., Michenaud, J.-P. & Gonze, X. Dynamical atomic charges: The case of ABO_3 compounds. *Phys. Rev. B* **58**, 6224–6239 (1998).
25. Antons, A., Neaton, J. B., Rabe, K. M. & Vanderbilt, D. Tunability of the dielectric response of epitaxially strained $SrTiO_3$ from first-principles. *Phys. Rev. B* **71**, 024102 (2005).
26. Giustino, F. & Pasquarello, A. Infrared spectra at surfaces and interfaces from first principles: Evolution of the spectra across the Si(100)–SiO_2 interface. *Phys. Rev. Lett.* **95**, 187402 (2005).
27. Wu, X., Stengel, M., Rabe, K. M. & Vanderbilt, D. Predicting polarization and nonlinear dielectric response of arbitrary perovskite superlattice sequences. *Phys. Rev. Lett.* **101**, 087601 (2008).
28. Seriani, N., Jin, Z., Pompe, W. & Colombi Ciacchi, L. Density functional theory study of platinum oxides: From infinite crystals to nanoscopic particles. *Phys. Rev. B* **76**, 155421 (2007).
29. Saad, M. M. *et al.* Intrinsic dielectric response in ferroelectric nano-capacitors. *J. Phys. Condens. Matter* **16**, L451–L456 (2004).
30. Tilley, D. R. & Zeks, B. Landau theory of phase transitions in thick films. *Solid State Commun.* **49**, 823–827 (1984).
31. Ghosez, P. & Rabe, K. M. Microscopic model of ferroelectricity in stress-free $PbTiO_3$ ultrathin films. *Appl. Phys. Lett.* **76**, 2767–2769 (2000).
32. Giustino, F. & Pasquarello, A. Theory of atomic-scale dielectric permittivity at insulator interfaces. *Phys. Rev. B* **71**, 144104 (2005).

Acknowledgements

This work was supported by the Department of Energy SciDac programme on 'Quantum simulations of materials and nanostructures', grant number DE-FC02-06ER25794 (M.S. and N.A.S.), and by ONR grant N00014-05-1-0054 (D.V.). Calculations were carried out at the San Diego Supercomputer Center and at the National Center for Supercomputer Applications.

Additional information

Reprints and permissions information is available online at http://npg.nature.com/reprintsandpermissions. Correspondence and requests for materials should be addressed to N.A.S.